Structure and light emission of swirling flames produced by pure hydrogen injection in cross-flow

Nicolas Vaysse, D. Durox, Preethi Rajendram Soundararajan, Ronan Vicquelin, Sébastien Candel, Antoine Renaud

Structure and light emission of swirling flames produced by pure hydrogen injection in cross-flow

N. Vaysse*[1], D. Durox[1], P. Rajendram Soundararajan[1], R. Vicquelin[1], S. Candel[1], and A. Renaud[1]

[1]Laboratoire EM2C, CNRS, CentraleSupélec, Université Paris-Saclay, 3, rue Joliot Curie, 91192 Gif-sur-Yvette cedex, France

Abstract

The path towards carbon-free aeronautical propulsion and power generation necessitates the adoption of new fuels. Among them, hydrogen offers a higher specific energy and its combustion in air produces no carbon compound. However, hydrogen flames raise two main issues: first, their high burning velocity promotes flashback, and secondly, NOx emissions are favored by the high adiabatic temperatures of these flames. To control these two phenomena, hydrogen and air must be quickly premixed to avoid hotspots, and the mixing has to be lean to reduce the flame temperature and NOx formation. From an industrial perspective, the flame has to be stabilized at a distance from the solid boundaries, which can be achieved using swirling flows. In this work, experiments are performed on a single-sector burner, already used to study premixed and spray hydrocarbon flames. The atomizer in the spray version of the burner is replaced by a new cross-flow injection system to produce pure hydrogen-air flames while taking into account those requirements. This injection scheme is investigated by exploring the domain of operation and analyzing the flame structures through light emission imaging and velocity measurements. Mixing under cold flow conditions is examined using laser tomography to determine the equivalence ratio distributions at the injector outlet. These systematic experiments help define operating conditions and design parameter ranges of interest.

Introduction

Injection is a crucial issue for the replacement of hydrocarbons by hydrogen in combustion. The large burning velocity of hydrogen in air makes it prone to flashback and its high flame temperature may potentially enhance NOx formation by the thermal oxidation mechanisms [1]. For industrial applications, the stabilization of lifted flames is targeted in order to reduce thermal loads on the injector unit and combustor structure. Another issue is to make sure that the flame established in the burner will be sufficiently well mixed and lean to eliminate regions of nearly stoichiometric conditions, reduce burning temperatures and limit NOx emissions.

Targeting these objectives, several injection geometries have been investigated recently in order to enhance mixing while controlling flashback. The flame stabilization can be obtained using injectors equipped with a central bluff body. This method allows flame anchoring of premixed methane flames enriched with hydrogen [2] with shapes evolving from wall-attached to bluff-body attached shapes as the hydrogen content is increased. In premixed configurations, axial air injection at high speed [3–5] in combination with swirl [6] have been shown as possible ways to increase the resistance to flashback. While axial air injection helps to lower the flashback limit of premixed hydrogen flames [4] while ensuring a sufficient mixing that maintains low NOx emissions [3, 5], swirling flows may enable to reduce wall boundary layer-induced flashback[6]. Double-swirl coaxial configurations operating at high hydrogen swirl and outlet velocity [7, 8] give rise to lifted flames that show promise. When the hydrogen nozzle is placed in recess with respect to the air outlet, the lifted flame domain is augmented [8].

The central idea of the present investigation is to combine a swirled air flow with transverse injection of hydrogen to enhance mixing and anchor the flame at a distance from the injection unit. A somewhat equivalent system has been used for oxy-colorless distributed combustion applied to mixtures of methane with hydrogen [9]. The flame can be stabilized at a distance from the injector outlet by the rotation imparted to the flow by a swirler thus reducing thermal loads on the chamber backplane and injection system. The radial injection of hydrogen in a strong helicoidal airflow is aimed at augmenting mixing to form a nearly homogeneous mixture ratio distribution that will be sufficiently lean to avoid NOx formation. This late-stage premixing is meant to lower the risks of flashback, as it has been observed in micro-mix combustors, featuring a multiplicity of cross-flow hydrogen injection units [10].

One practical difficulty with hydrogen flames is that they are barely visible. It is however possible to examine their light emission in the near UV associated with OH^* emission at 308 nm, and that of water vapor in the red and near-infrared regions as well as some broadband blue emission [11–13]. It has been shown that this blue emission can be due to excited water molecules [14] or to hydrogen peroxide [15]. In all cases, this emission

*Corresponding author: nicolas.vaysse@centralesupelec.fr

can be used as a tracer of the burnt gas region while OH^* remains in the flame front due to the quick desintegration of hydroxyl radicals.

This article begins with a brief presentation of the experimental facility and injection unit designated in what follows as CFI-X (eXperimental Cross Flow Injector). The level of premixing is first investigated using correlations for jets in crossflow and tomographic planar images at the injector outlet. It is then shown that detached flames can be obtained for a broad range of conditions. A lifted flame structure is then analyzed using emission imaging and velocity measurements.

Experimental setup

The experimental system is derived from the SICCA-Spray setup [16], previously used to study swirled premixed and spray hydrocarbon flames. The hollow cone spray atomizer is here replaced by a crossflow injection head with identical external dimensions (Fig. 1c). The injector enables gaseous hydrogen injection in the swirled air flow through six radial ports of diameter $d_i = 1.5$ mm. The mass flow rates of air and hydrogen are controlled by *Bronkhorst* EL-FLOW meters. One key parameter that is widely used to control jets in cross-flow is the hydrogen/air momentum flux ratio calculated in the vicinity of the injection ports [17]:

$$J = \rho_{H_2} v_{H_2}^2 / \rho_a v_a^2 \quad (1)$$

This ratio may be linked to the square of the equivalence ratio $J = \kappa \phi_g^2$ where κ may be expressed in terms of the mass stoichiometric ratio s, the density ratio ρ_{H_2}/ρ_a and of geometrical characteristics of the injection unit. The bulk velocities v_{H_2} and v_a are respectively those of the hydrogen jet and of the airflow in the injection section. In this work, the values of thermal power and equivalence ratio belong to the following ranges $\mathcal{P}_{th} \in [0.9; 5.3]$ kW and $\phi_g \in [0.2; 0.68]$, resulting in J values ranging from 0.03 to 0.35. The recess $h_r = 11.1$ mm represents the distance between the hydrogen ports and the injector outlet (Fig. 1c).

The airflow passes through a tangential swirler designated as 707, featuring a conventional swirl number $S = 0.60$ and pressure loss coefficient $\sigma = \Delta p / [(1/2)\rho U_b^2] = 3.25$ [18], where U_b is the axial bulk velocity at the injector outlet. The combustion chamber is constituted by a quartz tube with an internal diameter of $d_c = 68.5$ mm and length $l_c = 150$ mm (Fig. 1a).

Flame images are obtained using a *Princeton Instruments* PI-MAX4 intensified camera. An Asahi Spectra XBPA310 optical bandpass filter centered on 310 nm is used to record OH^* chemiluminescence emission from the flame. For burnt gases visualization, this filter can be replaced by a glass plate to eliminate emission in the UV range. A consumer-grade camera covering the visible spectrum is employed to capture natural light

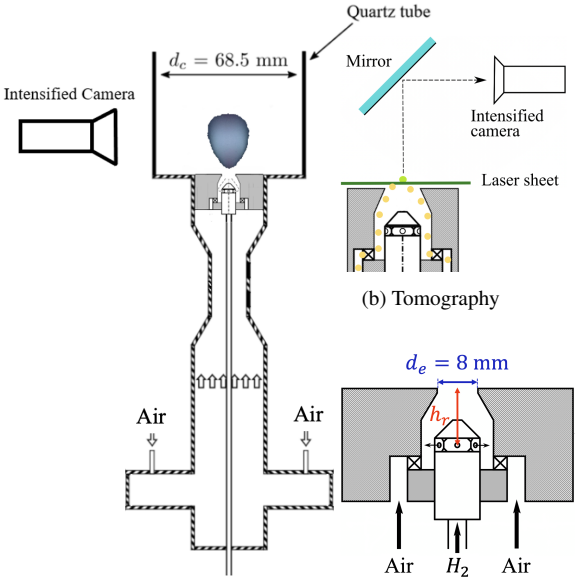

Figure 1: Experimental setup, adapted from [16]: full burner for (a) flame visualization, (b) tomography measurements, and (c) CFI-X with atomizer replaced by the crossflow injection head.

emission. Mean light emission images are processed using an Abel deconvolution and contours are determined with the Otsu thresholding method. The average light emission images are formed by accumulating 30 frames, each of them recorded with a gate width of 500 µs.

Flow transverse cuts are obtained by tomographic visualizations (Fig. 1b). In this setup the cylindrical quartz tube is removed to avoid parasitic light reflections. The airflow is seeded with small oil droplets (mean diameter 2.6 µm) and a laser sheet is formed at 1 mm above the injector outlet using a set of divergent and convergent lenses. The Stokes number is low (0.22), which means that the droplets are well entrained by the airflow. Images of the light scattered by the droplets are recorded under cold flow conditions with the same intensified camera PI-MAX4, using a mirror placed at 45° above the burner. The measurements were made at a constant air flowrate to guarantee a constant flowrate of droplets, whatever the equivalence ratio examined, $\phi_g = 0$ (no hydrogen), $\phi_g = 0.20$, $\phi_g = 0.42$ and $\phi_g = 0.68$. The seeding system is described in [19].

The tomographic light scattering images are used in what follows to determine the local equivalence ratio distribution ϕ_l and compare this quantity with the global equivalence ratio ϕ_g defined by the operating conditions. This is accomplished as follows. It is first noted that the oil droplet cloud can be considered monodisperse so that the Mie scattering intensity from a pixel in the tomographic images can be assumed to be proportional to the droplets' volumetric number density. Given that the number of droplets at a particular point is propor-

tional to the amount of seeded air reaching this point, this yields:

$$I_{Mie}(x,y) \propto \frac{q_{sa}(x,y)}{q_{sa}(x,y)+q_{ua}(x,y)+q_{H2}(x,y)}, \quad (2)$$

where I_{Mie} is the Mie scattering signal corresponding to a given pixel, q_{sa} is the volume flow rate of seeded air through that point, q_{ua} the volume flow rate of unseeded air (due to the recirculation of external air in the vicinity of the burner axis) and q_{H2} the volume flow rate of hydrogen. Applying this to images recorded without hydrogen injection (air-only, superscript ^{ao}) and to images with hydrogen injection (superscript ^{H2}), one obtains:

$$I^{ao}_{Mie}(x,y) = K\frac{q^{ao}_{sa}(x,y)}{q^{ao}_{sa}(x,y)+q^{ao}_{ua}(x,y)}, \quad (3)$$

$$I^{H2}_{Mie}(x,y) = K\frac{q^{H2}_{sa}(x,y)}{q^{H2}_{sa}(x,y)+q^{H2}_{ua}(x,y)+q_{H2}(x,y)}, \quad (4)$$

where K is a proportionality constant that depends on the recording conditions and on the way flow seeding is performed and is therefore the same for the two images. Under the hypothesis, which is admittedly an approximation, that hydrogen injection does not change the airflow distribution, $q^{H2}_{sa}(x,y) \simeq q^{ao}_{sa}(x,y)$ and $q^{H2}_{ua}(x,y) \simeq q^{ao}_{ua}(x,y)$. One can then write the following relation:

$$\frac{I^{ao}_{Mie}(x,y)}{I^{H2}_{Mie}(x,y)} - 1 = \frac{q_{H2}(x,y)}{q_{sa}(x,y)+q_{ua}(x,y)} = \frac{\phi_l(x,y)}{\nu_a}, \quad (5)$$

where ϕ_l is the local equivalence ratio and $\nu_a = 2.36$ is the molar stoichiometric coefficient. After background subtraction, the tomographic images are thus processed in this fashion to obtain estimates of ϕ_l.

Mixing of hydrogen with air

Before examining tomographic images, it is first instructive to use correlations from the many studies of jets injected in crossflow and examine the jet centerline trajectory. The initial location of this line is essentially a function of the momentum flux ratio [20] and provides an indication on the penetration of the jet. The geometry of the jet may be approximated by Ivanov's model:

$$x/D = J^{1.3}\,(z/D)^3 + (z/D)\cot(\delta_j) \quad (6)$$

where x and z are respectively the tangential and normal coordinates of the jet center point in a reference frame where the origin is attached to one of the hydrogen inlets. One advantage of this model is that it accounts for the crossflow angle δ_j. It is interesting here because the hydrogen jet penetrates first in the swirling air, where δ_j is close to 90° before entering the converging section in the injection unit. The trajectories plotted in Fig. 2 are calculated assuming an initially uniform air velocity magnitude and an initially zero radial velocity component in the injection ports region, and parallel to the wall in the channel region. The velocity magnitude is computed as $v_{air} = (v_z^2 + v_\theta^2)^{1/2}$ where the axial component v_z is obtained using the volumetric air flow rate and the radial component v_θ designates a mean tangential velocity computed using swirler geometry and assuming a linear radial velocity profile in the swirling flow.

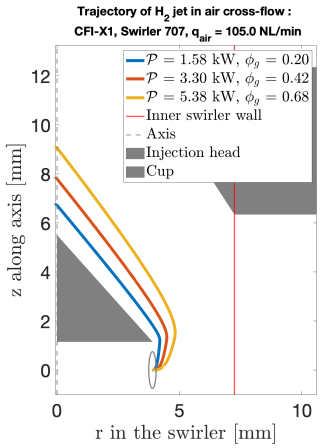

Figure 2: Simulation of the hydrogen jet trajectory for three different equivalence ratios: 0.20 ($J = 0.03$), 0.42 ($J = 0.13$) and 0.68 ($J = 0.35$).

The computed trajectories penetrate to a finite distance in the annular channel between injection head and cup and the jets are then quickly entrained with the airflow to form a central region of mixed hydrogen and air. The hydrogen jet centerline location moves away from the injection head as the global equivalence ratio is increased because the momentum flux ratio changes like ϕ_g^2. This theoretical analysis does not take into account the turbulence created by the swirl of the airflow nor the fluid interactions created by the air jets that emerge almost opposite the hydrogen jets, at the bottom of the injector (see Fig. 1c).

In addition to jet penetration, it is also interesting to look at the mixing of hydrogen and air resulting from the strong shear between the two streams. This is best accomplished by making use of tomographic visualizations. The previous analysis indicates that one can expect to find a central region where hydrogen and air are mixed. This is now verified by examining the tomographic images shown in Fig. 3. All images are obtained with the same camera settings and with the same flowrate of droplets. The first row corresponds to the raw images. The second row gives the local equivalence ratio ϕ_l deduced from expression (5) while the third row shows the local equivalence ratio divided by the global value defined by injection conditions ϕ_l/ϕ_g. A perfect mixing assures that the latter quantity would be equal to unity. This is not so however. Hydrogen mixes with a certain amount of air but the central region is still hydrogen-rich and some of the air flows around the mixed hydrogen-air region. This is probably a sign that the penetration of the hydrogen jet in the airflow and the residence time for turbulent mixing are insufficient.

It is worth noting that further mixing will take place outside the injector before the flame and that some additional mixing takes place with the recirculated stream. Although a level of premixing is achieved, the presence of a mixture ratio gradient indicates that some combustion will take place in a non-premixed mode. The tomographs show that the global equivalence ratio highly influences the resulting values of local equivalence ratio. Probability density functions are computed based on these images for the reduced equivalence ratio ϕ_l/ϕ_g. The results are displayed in Fig. 4.

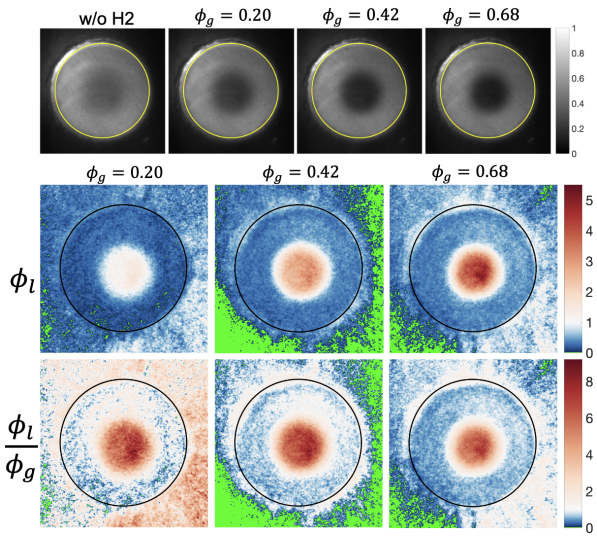

Figure 3: Tomography at the burner outlet: Raw images obtained (from left to right) without hydrogen injection, with global equivalence ratios $\phi_g = 0.20$, 0.42 and 0.68. Second row: maps of local equivalence ratio ϕ_l. The white colour corresponds to stoichiometric conditions, and the green pixels to uninterpretable points where computed ϕ_l is negative. Third row: maps of reduced equivalence ratio ϕ_l/ϕ_g. The white colour corresponds to $\phi_l = \phi_g$. Yellow and black circles represent the burner outlet.

One may also want to study how close the resulting local equivalence ϕ_l is to ϕ_g, in order to better control the temperature of the flame. Figure 4 shows that $\phi_g = 0.20$ gives a peak centered on $\phi_l = \phi_g$. With $\phi_g = 0.68$, the probability density peak is located at only half the global equivalence ratio. By setting an intermediate global equivalence ratio $\phi_g = 0.42$ (orange curve), one obtains a distribution closer to $\phi_l = \phi_g$, that is as thin as the distribution obtained with $\phi_g = 0.68$ (top of Fig. 4). Thus, the value $\phi_g = 0.42$ optimizes the premixing.

The previous results extracted from a much larger database give some insights on the influence of momentum flux ratio J through variations of the global equivalence ratio ϕ_g. They also give clues on the premixing of air and hydrogen gives and on the location of fresh reactants.

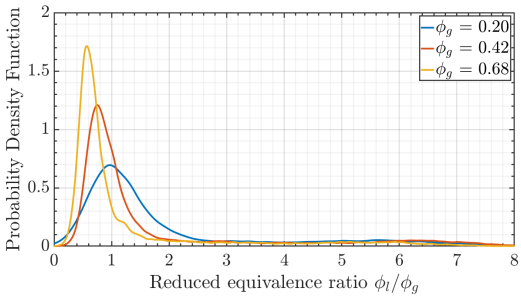

Figure 4: Probability Density Functions of the local and reduced equivalence ratios ϕ_l and $\phi_r = \phi_l/\phi_g$ approximated inside the hole zone for global equivalence ratios: 0.20 ($J = 0.03$), 0.42 ($J = 0.13$) and 0.68 ($J = 0.35$).

Flame shapes In reactive conditions, the investigated powers and equivalence ratio led to three different types of stable flames: a "V" flame attached to the injector, a thin lifted flame and another lifted flame, obtained at higher equivalence ratio, that features a much thicker and open flame brush. Abel-inverted OH^* images of these three flames are shown in Fig. 5. The less premixed condition $\phi_g = 0.20$ gives a V-attached flame, whose conical flame front can be understood as a quasi diffusion flame front. The $\phi_g = 0.68$ case, characterized by a better premixing, leads to the widest flame.

It is next interesting to get a general idea of the effect of operating conditions on the flame configuration. This information is synthesized in Fig. 5 where the flame shapes are categorized as a function of the bulk velocity U_b and global equivalence ratio ϕ_g. The transition between "V"-attached flames and lifted flames at $\phi_g = 0.42$ is linked to U_b since flames obtained below $30\,\mathrm{m\,s^{-1}}$ are attached while they are detached from the injector for $U_b > 40\,\mathrm{m\,s^{-1}}$. The transition between the two flame shapes gives rise to unstable flames featuring a cyclic attachment and detachment. Globally, the lift-off is driven by the thermal power, since all the flames below 3 kW remain attached while increasing the power beyond this threshold induces a lift-off.

Structure of lifted hydrogen flames

It is interesting to examine a detached flame case obtained by fixing the equivalence ratio at 0.42 ($J = 0.13$) and setting the thermal power at $\mathcal{P}_{th} = 4.6$ kW (Fig. 6). The flame is anchored at a distance from the outlet lips and the combustor backplane. It corresponds to a lifted thin flame in Fig.5. From the visible light image (Fig. 6a), one observes a pale blue emission region that corresponds to the radiation of hydrogen flames in the blue [14]. The image also features a slight emission in the red corresponding to H_2O mainly emitting between 600 and 680 nm [11]. A different view of the flame is provided by the line-of-sight integrated OH^* chemiluminescence displayed in Fig. 6b. The excited hydroxyl radical is essentially present in the reaction layer where chemical conversion takes place. In this image, the

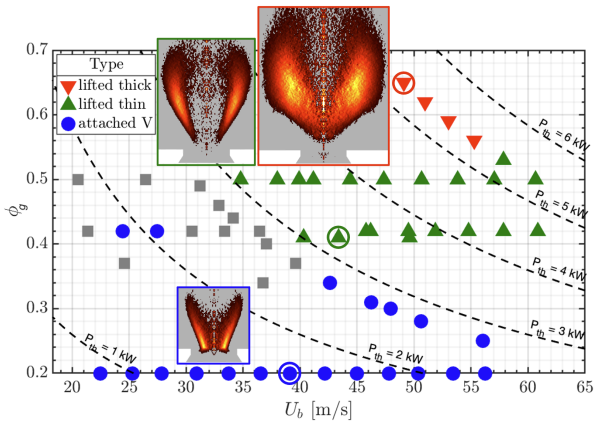

Figure 5: Types of flame shapes obtained with the SICCA-H2 setup as a function of the fresh stream bulk velocity U_b and global equivalence ratio ϕ_g. The gray squares correspond to unstable flames. Dashed lines represent iso-thermal power $\mathcal{P}_{th}$. Abel-inverted OH* images of the flames corresponding to premixing measurements (circled points) are represented.

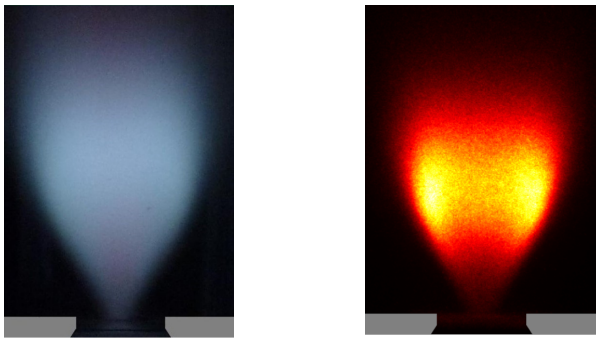

(a) Visible natural light (b) OH* light emission

Figure 6: Hydrogen/air flames obtained with the SICCA-H2 setup at thermal power $\mathcal{P}_{th} = 4.6$ kW and global equivalence ratio $\phi_g = 0.42$. (a) Visible light emission integrated over the line of sight. (b) OH* chemiluminescence, line-of-sight integrated.

flame front is clearly detached from the injector outlet and the maximum emission intensity is around 12 mm above the backplane. The level of Abel-inverted OH* radiation originating from the inner core is low indicating that this region is occupied by recirculating combustion products that anchor the flame (Fig. 7a). It is interesting to note that the OH* Abel transformed images notably differ from the visible light emission images and that they provide a better indication on the mean position and shape of the chemical conversion region in the flame.

Using a glass plate to cut the UV range one obtains an image of the visible light emission that may be assumed to be radiated by the hot products. The visible emission ceases when the products are cooled down away from the flame. This may then be used to extract the mean location of the high temperature burnt gases trough an Abel transform (Fig. 7b). The contour of OH* emission is superimposed on this image. For the lifted

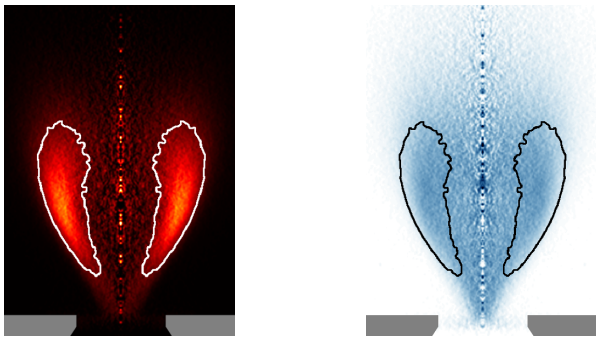

(a) OH* light emission (b) Visible light emission

Figure 7: Abel-inverted images of the light radiated in a lifted thin flame ($\mathcal{P}_{th} = 4.6$ kW and $\phi_g = 0.42$) (a) by OH* radicals and (b) in the visible range. The contour of the Abel transformed OH* image obtained with Otsu method is superimposed on both images.

thin flame, the visible zone includes the hot products region and the flame itself. It occupies the central region forming a core that extends into the injector as a result of the inner recirculation induced by the swirling flow.

Some indications on the role of the flow in the positioning of the lifted flame front may be deduced from Laser Doppler Anemometry using micronic oil droplets to seed the cold flow. The profiles shown in Fig. 8 are obtained at a distance of 2 mm from the outlet. The droplets are vaporized at 600K explaining the absence of data points in the central region ($r < 2$ mm) occupied by hot combustion products. The axial velocity reaches its maximum (90 m s^{-1}) at a radial distance of about 3 mm, it drops down with r, and also diminishes in the central region. The low values taken by flow velocity near the axis indicate the presence of an internal recirculation zone but the lack of data in this region does not allow more precise identification of this zone. Results for the tangential component of the velocity reflect the presence of the swirling flow. This velocity component also features a maximum (50 m s^{-1}) at a radial distance corresponding to the outlet lip. The velocity profiles indicate that the mean flow structure is fairly symmetric. The light intensity of the Abel-inverted OH* signal, which locates the flame in this section, reaches its maximum value in the core region where the seeding droplets disappear and where the axial velocity drops down. These observations are consistent with the flame structure configuration appearing in Fig. 7b. The axial velocity rms fluctuation plotted in Fig. 8 indicate the presence of two shear regions, the first is between the fresh stream originating from the injector and the inner recirculation flow, the second at a larger radial distance between the jet of fresh reactants and the outer recirculation zone formed near the backplane and the combustor wall. The velocity measurements also indicate that the flame is stabilized in the shear zone separating the core region formed by the inner recirculation zone (IRZ), and

the fresh stream coming out of the injector. No reaction is taking place in this second shear zone.

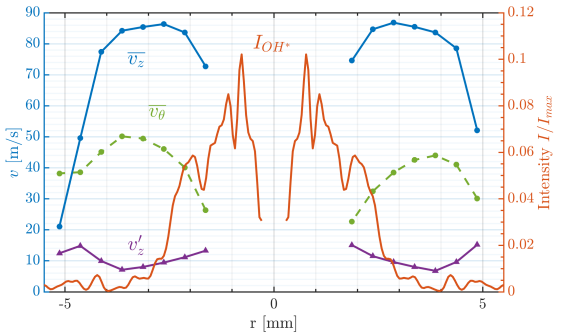

Figure 8: Mean axial and tangential velocity fields measured at 2 mm above the burner outlet in the lifted flame ($\mathcal{P}_{th} = 4.6$ kW and $\phi_g = 0.42$). The purple curve is the RMS axial velocity field. The orange curve is the OH^* intensity on the Abel-inverted image of the flame. It has been normalized by the maximum intensity in the flame. The OH^* signal has been cut on the axis to eliminate Abel inversion artifacts.

Conclusions

Experiments are carried out on a system in which hydrogen is injected in cross-flow in a radial swirling injector configuration. The data indicates that a level of premixing can be achieved and that this level and spatial extent depend on the momentum flux ratio and can be varied in the present experiments by changing the global equivalence ratio. The equivalence ratio distributions at the burner outlet deduced from tomographic images indicate that the premixed region is rich around the axis and surrounded by an annular lean premixture. A systematic exploration of the domain of operation indicates that detached flames are obtained for high thermal powers. The reactive region is detached from solid boundaries. An analysis of the light radiated by the flame in the visible range and in the UV provides insights on the structure of these flames. This, in combination with velocity measurements, indicates that the flame is anchored in the shear layer between the jet of fresh reactants formed by the injector and the internal recirculation zone. When the system is operated at a higher global equivalence ratio, the lifted flame volume is augmented and the flame occupies a larger portion of the chamber cross section.

Acknowledgements

This work was partially supported by the FlyHy project of the Agence Nationale de la Recherche (ANR-21-CE05-0008).

References

[1] Zeldovich, Y., 1946. *Acta Physicochem USSR*, pp. 577–628.

[2] Aguilar, J. G., Æsøy, E., and Dawson, J. R., 2022. *Combustion and Flame,* ***245***(112323), Nov.

[3] Reichel, T. G., Terhaar, S., and Paschereit, O., 2015. *J Eng Gas Turbines Power,* ***137***(7), July, p. 071503.

[4] Sattelmayer, T., Mayer, C., and Sangl, J., 2016. *J. Eng. Gas Turbines Power,* ***138***(1), Jan., p. 011503.

[5] Reichel, T. G., Terhaar, S., and Paschereit, C. O., 2018. *Journal of Propulsion and Power,* ***34***(3), May, pp. 690–701.

[6] Baumgartner, G., and Sattelmayer, T., 2013. "Experimental Investigation of the Flashback Limits and Flame Propagation Mechanisms for Premixed Hydrogen-Air Flames in Non-Swirling and Swirling Flow". In ASME, Paper No: GT2013-94258, V01AT04A010; 10 pages.

[7] Leroy, M., Mirat, C., Renaud, A., and Vicquelin, R., 2022. *Journal of Engineering for Gas Turbines and Power,* ***145***(2), Nov., p. 021021.

[8] Marragou, S., Magnes, H., Poinsot, T., Selle, L., and Schuller, T., 2022. *Int J Hydrogen Energy,* ***47***(44), May, pp. 19275–19288.

[9] Karyeyen, S., Feser, J. S., and Gupta, A. K., 2019. *Fuel,* ***253***, Oct., pp. 772–780.

[10] Dahl, G., and Suttrop, F., 1998. *International Journal of Hydrogen Energy,* ***23***(8), Aug., pp. 695–704.

[11] Gaydon, A. G., 1974. *The Spectroscopy of Flames*, Vol. p.103. Springer Netherlands, Dordrecht.

[12] Schefer, R., Kulatilaka, W., Patterson, B., and Settersten, T., 2009. *Combustion and Flame,* ***156***(6), June, pp. 1234–1241.

[13] Fiala, T., Sattelmayer, T., Gröning, S., Hardi, J., Stützer, R., Webster, S., and Oschwald, M., 2017. *Journal of Propulsion and Power,* ***33***(2), Mar., pp. 490–500.

[14] Padley, P. J., 1960. *Trans. Faraday Soc.,* ***56***, p. 449.

[15] Vanpee, M., and Mainiero, R. J., 1979. *Combustion and Flame,* ***34***, Jan., pp. 219–230.

[16] Prieur, K., Durox, D., Vignat, G., Schuller, T., and Candel, S., 2017. "Experimental determinations of Flame Describing Functions of swirling spray flames". In Colloq. INCA Châteaufort Fr.

[17] Kolla, H., Grout, R. W., Gruber, A., and Chen, J. H., 2012. *Combustion and Flame,* ***159***(8), Aug., pp. 2755–2766.

[18] Vignat, G., Durox, D., Prieur, K., and Candel, S., 2019. *Proceedings of the Combustion Institute,* ***37***(4), Jan., pp. 5205–5213.

[19] Durox, D., Ducruix, S., and Lacas, F., 1999. *Experiments in Fluids,* ***27***(5), Oct., pp. 408–413.

[20] NATO, and AGARD, eds., 1993. *Computational and Experimental Assessment of Jets in Cross Flow*. No. 534 in AGARD Conference Proceedings. AGARD, Neuilly-sur-Seine.